ELSEVIER

Contents lists available at ScienceDirect

Sensors and Actuators: A. Physical

journal homepage: www.journals.elsevier.com/sensors-and-actuators-a-physical





Extension-type flexible pneumatic actuator with a large extension force using a cross-link mechanism based on pantographs

So Shimooka a,*, Kazuma Tadachi b, Tetsushi Kamegawa a

- ^а Faculty of Environmental. Life. Natural Science and Technology. Okayama University. 3-1-1 Tsushima-naka. Kita-ku. Okayama. Japan
- ^b Mechanical and Systems Engineering Program, School of Engineering, Okayama University, 3-1-1, Tsushima-naka, Kita-ku, Okayama, Japan

ARTICLE INFO

Keywords: Soft robot Extension soft actuator Link mechanism Pantograph Attitude control

ABSTRACT

In this study, we propose an extension-type flexible pneumatic actuator (EFPA) with a high extension force and no buckling. In a previous study, soft actuators that extended in the axial direction by applying a supply pressure were unable to generate the extension's pushing force because the actuators buckled owing to their high flexibility. To generate a pushing force, the circumferential stiffness of an extension-type flexible soft actuator must be reinforced. Therefore, a cross-linked EFPA (CL-EFPA) was developed, inspired by a pantograph that restrains the EFPA three-dimensionally using the proposed link mechanism. The proposed CL-EFPA consists of three EFPAs and a cross-linking mechanism for integrating each EFPA circumference. The pushing force of the CL-EFPA is approximately 3.0 times compared with that generated by the previous EFPA with plates to restrain its plane. To perform various bending motions, attitude control was performed using an analytical model and a system that included valves, sensors, and controllers.

1. Introduction

Soft actuators, such as McKibben-type rubber artificial muscles and inflatable actuators, have been extensively researched and developed [1-7]. Actuators are used in power-assist suits, robotic arms, and rehabilitation devices [1,5,8]. Actuators have several advantages, including their lightweight, low cost, high flexibility, and back-drivability characteristics. In addition, the artificial rubber muscles generate large force for contraction [9,10]. The contraction ratio of the previous actuator is approximately 30-40 %. Therefore, artificial rubber muscles are required to realize power-assist suits and robotic arms because these actuators have small moving areas. On the other hand, many soft actuators with high extension ratios (150-300 %) have been proposed and developed [11-23]. Extension-type soft actuators are manufactured using a silicone rubber tube covered in a bellows sleeve and fiber [11–13], plastic film [14–16], and melt deposition modeling [17–25]. In addition, extension-type soft actuators without rubber materials have been proposed using springs and plastic bellows [26,27]. Unlike rubber artificial muscles, soft actuators can extend while maintaining a constant flexibility even under high pressure (supply pressure of \geq 300 kPa) [10, 12,28]. Soft actuators are capable of both extension and bending motions with a larger moving area [20–22, 28–30]. However, soft actuators using rubber materials cannot generate a sufficient extension force, that is, the pushing force. This is because soft actuators buckle owing to their high flexibility and low stiffness. In previous studies, the lengths and bending angles of linear soft actuators were measured; however, the pushing forces of these actuators were not measured. The pulling and bending force of soft actuators were measured when they were decompressed from the extension state [12,27]. The pushing force of soft actuators is approximately 10 N [17,22,25]. It is difficult to use a soft actuator with a small force or extension ratio in industrial and welfare fields such as robotic arms and assist devices. If a soft actuator with a high extension ratio is developed that can generate a large pushing force similar to that of a pneumatic cylinder, a soft robotic arm that is lightweight and compact compared with typical industrial rigid robots and assist devices with high human friendliness can be realized to lift heavy objects. In particular, extension soft actuators must operate over a wider range of motion (compared with conventional soft actuators) and generate a pushing force while maintaining compactness and flexibility.

Inflatable actuators with plastic films can achieve a large pushing force (max. 300 N); however, they cannot return to their initial state upon decompression [13–16]. This is because inflatable actuators lack an elastic function. In addition, these actuators require a large cross-sectional area to prevent buckling and generate a pushing force.

E-mail address: shimooka@okayama-u.ac.jp (S. Shimooka).

^{*} Corresponding author.

Soft actuators focusing on pushing force have been proposed and developed [31–34]. In particular, the pushing force of a linear sleeve actuator using thermoplastic polyurethane (TPU) of 85 Shore A was obtained up to the maximum of 210 N (extension ratio 1.6 times) [34]. However, the study does not clarify whether the linear sleeve actuator can generate a large pushing force without buckling as its length increases or whether it can perform bending motions. It is necessary to improve the reproducibility and flexibility of the actuator if robotic arms and assist devices using various actuators are achieved.

In this study, we aimed to develop an extension-type soft actuator capable of generating a greater pushing force while maintaining flexibility. In addition, a soft actuator capable of generating a greater pushing force than a previous actuator was realized, despite having a longer initial length. In a previous study, a reinforced extension-type flexible pneumatic actuator (EFPA) with an extension ratio of 2.5 times (initial length is 200 mm) generated a pushing force of 180 N by applying a supply pressure using plastic plates [35]. However, the reinforced EFPA buckled, and its pushing force decreased when a supply pressure of \geq 250 kPa was applied while both ends of the actuator were fixed. To solve the buckling problem, a soft mechanism was considered that could generate a greater pushing force without buckling, even when a supply pressure of 500 kPa was applied. It is believed that the stiffness of the soft actuator is improved by applying three-dimensional constraints rather than by constraining the plane, such as inserting plastic plate uniformity.

2. Development of cross-link extension-type flexible pneumatic actuator

2.1. Construction of the CL-EFPA

In a previous soft actuator, the EFPAs were uniformly restrained using plastic plates, as shown in Fig. 1 [35].

The actuator buckled, and the pushing force decreased because it was restrained in only one plane, as shown in Fig. 2. In other words, buckling occurred more easily because the actuator was twodimensionally restrained. To generate a larger pushing force, it was necessary to reinforce the horizontal stiffness of the soft actuator. To reinforce the stiffness and generated force, soft actuators that combine an inflatable actuator and a link mechanism, such as scissors and tensegrity, have been proposed [36,37]. Although actuators can extend with pressurization, it is difficult to perform a bending motion owing to the restrain by the link mechanisms. Other tensegrity mechanisms [5, 38] have been used to achieve a large force and flexible motion. However, their structures are complex, and their motion design is difficult. Therefore, the stiffness of the soft actuator can be enhanced by extending the linkage mechanism into three dimensions to continuously constrain the outer circumference of each EFPA. This technique is expected to improve the pushing force of the actuator. To reinforce the stiffness of the actuator, we focused on the mechanism of the pantograph, which was used as a jack. The pushing force of the soft actuator

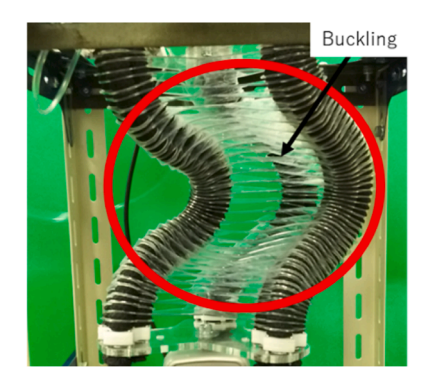


Fig. 2. View of buckling of previous soft actuator.

was improved while maintaining flexibility by restraining the EFPAs using a pantograph. The upper part of Fig. 3 shows the cross-linking mechanism expanded three-dimensionally based on the pantograph. The cross-link mechanism, made of 3D-printed parts to be inserted in each bellows of the EFPA and polyoxymethylene linkage to connect each 3D-printed part, was designed to have three EFPAs placed at 120° intervals. By connecting multiple linkage mechanisms and inserting them into each bellow of the EFPA, it is believed that the soft actuator can enhance its stiffness and prevent buckling in the horizontal direction.

Fig. 3 shows the CL-EFPA using the three EFPAs and the link mechanism. A single cross-linking mechanism in the CL-EFPA was inserted into the bellows sleeve of the EFPA every ten pitches, as shown in Fig. 3. To maintain the position of the EFPAs, each bellows sleeve of the EFPA was held using six cross-linking mechanisms and plastic plates. As shown in Fig. 3, the tested CL-EFPA had an initial height of 210 mm and a width of 197 mm. One link used in the linkage mechanism had a size of $5.5 \times 55 \times 3$ mm and a mass of 1.2 g. The initial length of each EFPA was set to 210 mm based on the previous reinforced EFPA. Each EFPA was positioned 90 mm from the center of CL-EFPA. The generated force and flexibility of the CL-EFPA could be adjusted by changing the insertion interval of the mechanism. The mass of the CL-EFPA was approximately 800 g.

2.2. Operating principles of CL-EFPA

The operating principles are as follows. When all the EFPAs were pressurized, the silicone rubber tube of the EFPA expanded in the radial and longitudinal directions. Each EFPA could extend longitudinally because it was deformed only in the axial direction by the bellows sleeve, as shown in Fig. 4. Each EFPA could be extended longitudinally even if the CL-EFPA deformed inward, owing to the mechanism shown in Fig. 4. When one or two EFPAs were pressurized, the CL-EFPA bent in the direction opposite to that of the pressurized EFPAs. Fig. 5 shows a transient view of the bending motion of the proposed CL-EFPA at various pressures on the right side of the EFPA. The bending directional angle α was defined as an angle from the x-axis of the actuator, and the bending

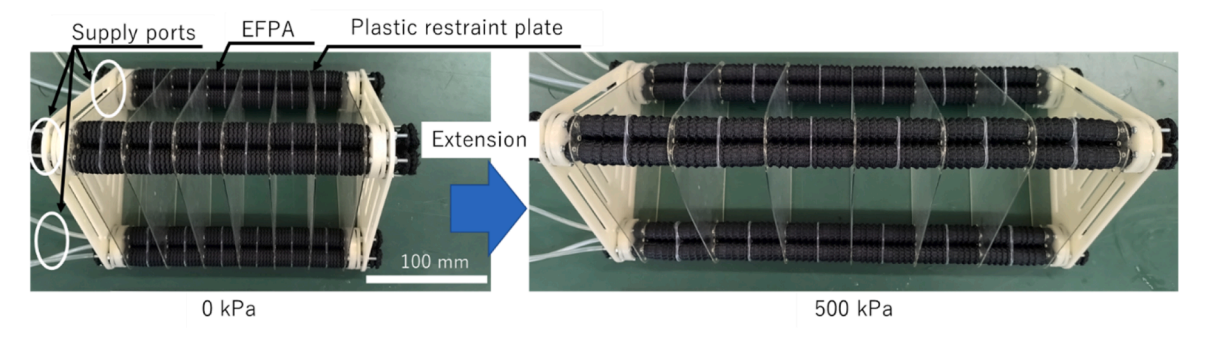


Fig. 1. Extension of previous soft actuator.

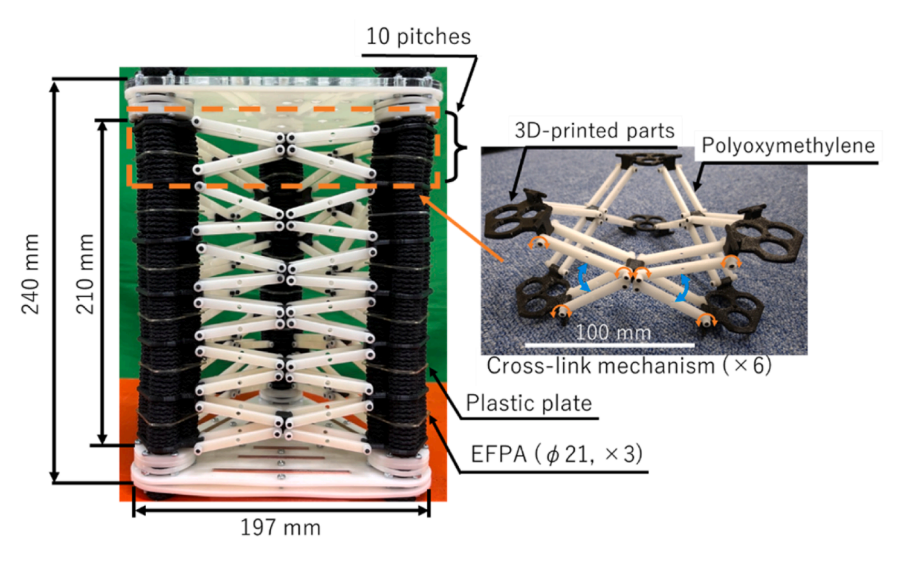


Fig. 3. Appearance of CL-EFPA.

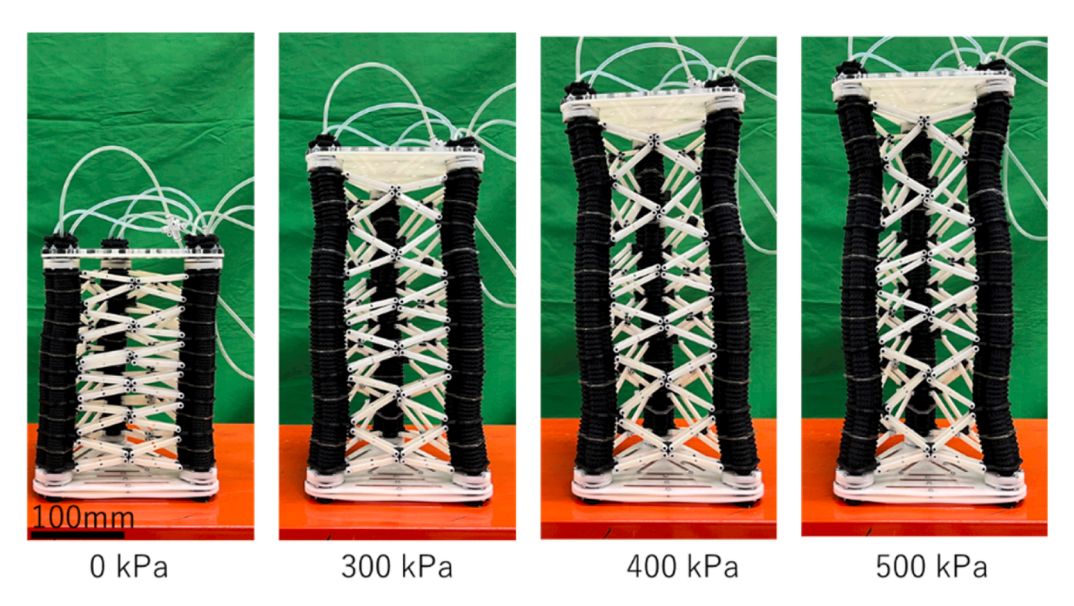


Fig. 4. Transient view of extension motion.

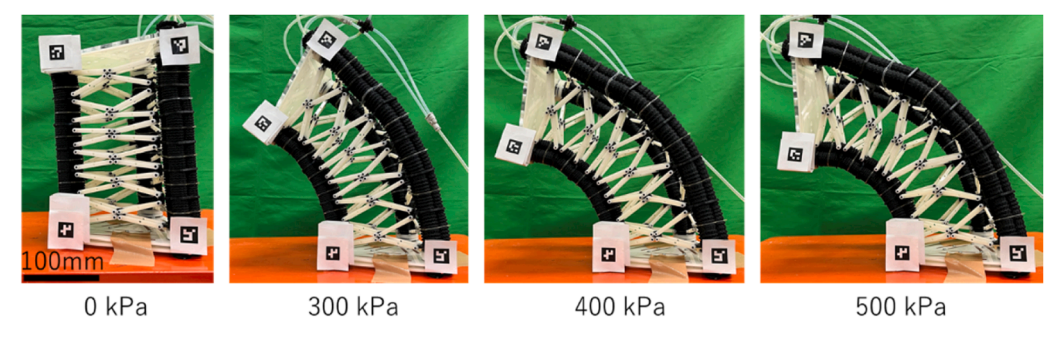


Fig. 5. Transient view of bending motion.

angle β was defined as an angle from the z-axis (Fig. 13). The bending and directional angles of the CL-EFPA could be adjusted by varying the pressure magnitude.

2.3. CL-EFPA characteristics

The extension and bending characteristics of CL-EFPA were investigated when each EFPA was pressurized. Fig. 6 shows the relationship between the pressure and displacement of the CL-EFPA when the three EFPAs were simultaneously pressurized. During the experiment, the

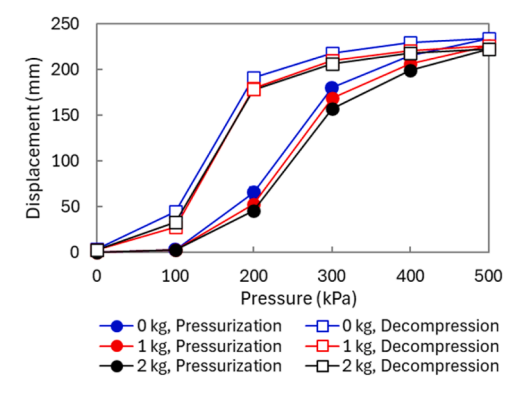


Fig. 6. Relationship between pressure and displacement.

displacement of the CL-EFPA was measured using a scale based on its initial length. The initial length of the CL-EFPA was approximately 210 mm. In addition, we performed experiments in which loads of 1 and 2 kg were applied to the top end of the CL-EFPA. The results indicated that the maximum displacement was 233 mm and the extension ratio was approximately 2.1 times. However, the extension of the EFPA required a supply pressure of more than 100 kPa because the silicone rubber tube cannot expand below this pressure. In addition, the relationship between the pressure and displacement showed considerable hysteresis. These problems are believed to be caused by the friction between the silicone rubber tube and the bellows sleeve inside the EFPA. The extension ratio of CL-EFPA (2.1 times) was smaller than that of a previous one (2.3 times) [35]. This implies that the longitudinal displacement of the actuator decreased because the EFPA was deformed inward into the proposed actuator through a cross-linking mechanism, as shown in Fig. 4. Therefore, to develop a CL-EFPA with a higher extension ratio, it is necessary to devise a cross-linking mechanism that does not deform the EFPA during extension.

According to the results of the extension motion with loads, the actuator achieved a consistent displacement without buckling, as shown in Fig. 2. The displacement of the actuator decreased with an increasing load. However, the displacement reduction decreased as the supply pressure increased. In the decompressed state, the actuator contracted more with each load than that without the load, owing to gravity.

Fig. 7 shows the relationship between the pressure and bending angle of the CL-EFPA. In this experiment, the bending angle was measured using image processing and Augmented Reality (AR) markers. The bending angle β was calculated using the coordinates obtained by the marker, as shown in Fig. 8. For the experiment shown in Fig. 6, the bending angle was also measured when a load was applied to the actuator as follows: In Fig. 7, each symbol and line represents the supply or exhaust pressure as well as one or two pressurized EFPAs. From this characteristic, it can be observed that the bending angles in the case of

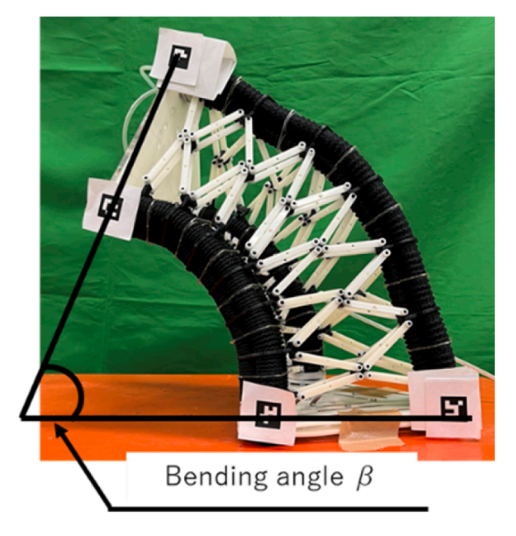


Fig. 8. Measurement of bending angle.

the two pressurized EFPAs were large. In the case of the extension of the two EFPAs, it was considered that the CL-EFPA could bend further because the generated force increased.

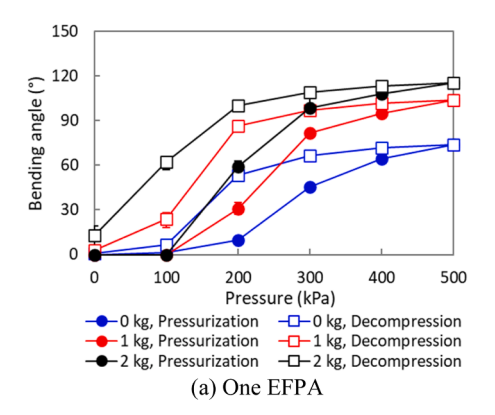
The results of the bending motion demonstrated that the bending angle of the actuator with the load was larger than that without it, which is similar to the results of the extension motion shown in Fig. 6. At a supply pressure of 200 kPa, dispersion in the bending angle was observed owing to the low stiffness of the actuator. This dispersion could be reduced by decreasing the insertion interval of the link mechanism.

3. Comparison with previous extension-type soft actuators

3.1. Subject of comparison

To evaluate the generated force and bending stiffness, the CL-EFPA was compared with previous extension-type soft actuators. Fig. 9(a) and (b) show the previously integrated EFPAs with and without large PET restraint plates, respectively. To increase the generated force, one of the previously integrated EFPAs had large PET restraint plates, as shown in Fig. 9(b) [35].

The length and number of pitches in the integrated EFPAs were the same as those in the CL-EFPA. In addition, the integrated EFPA with large restraint plates had small restraint plates inserted in steps of five pitches. Thus, the integrated EFPA, which increased the stiffness using large and small restraint plates, was compared with the proposed CL-EFPA.



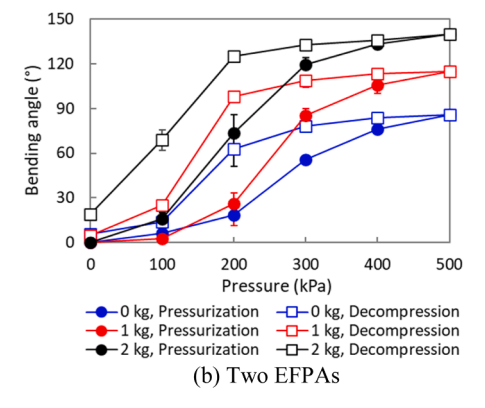


Fig. 7. Relationship between pressure and bending angle when applied to the EFPA.

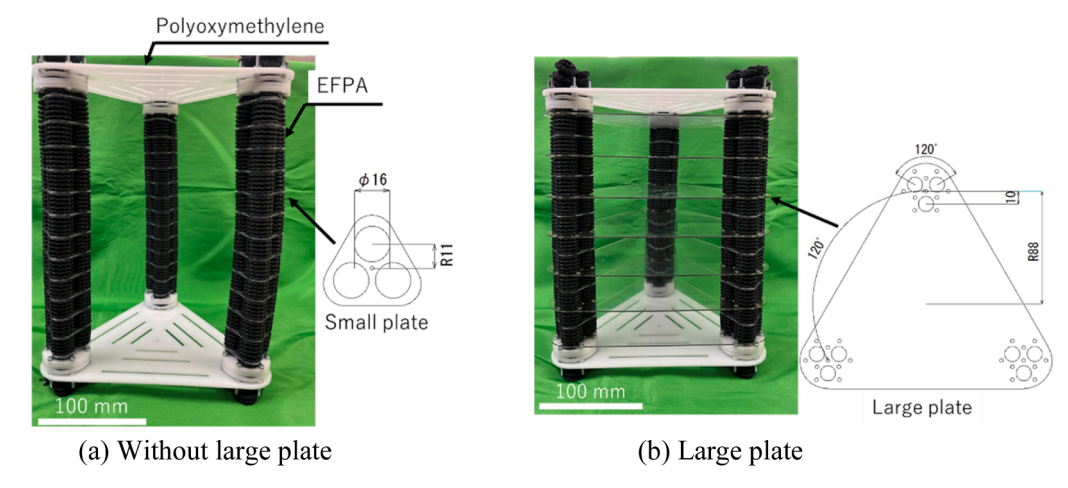


Fig. 9. Depictions of the previous model of integrated EFPA.

3.2. Characteristics of generated force in all soft actuators

The generated force, or pushing force of the soft actuator, was measured using three types of actuators, as shown in Figs. 3 and 9 shows the experimental setup used to measure the generated force (pushing force). Each EFPA was connected in series with a force gauge (NIDEC-SIMPO Corp., FGJN-50; resolution: 0.1 N). In addition, the upper end of the actuator was fixed to the base, while the lower end was connected to a fixed force gauge, allowing the pushing force to be measured at a 0 % extension rate. Each actuator was pressurized in increments of 50 kPa until it buckled, or at 500 kPa. In addition, they were decompressed from 50 kPa to 0 kPa, and the generated force was measured five times.

Fig. 11 shows the relationship between pressure and generated force of each actuator. In Fig. 11, each line and symbol denotes the generated force of each actuator when supply and exhaust pressures are applied to it. The values in the legend of Fig. 11 represent the maximum standard deviations for each measurement. It was observed that the force generated by each actuator increased as a function of the supply pressure. Although the actuators had different structures, the generated force of each actuator exhibited the same tendency up to 150 kPa. However, it was confirmed that the integrated EFPAs buckled, and their generated forces decreased when a supply pressure higher than 200 or 300 kPa was applied. The maximum generated forces of the integrated EFPAs with and without the large plate were approximately 83 and 37 N, respectively. The pushing forces under buckling in the two types of EFPAs were constant and did not increase further. However, the force

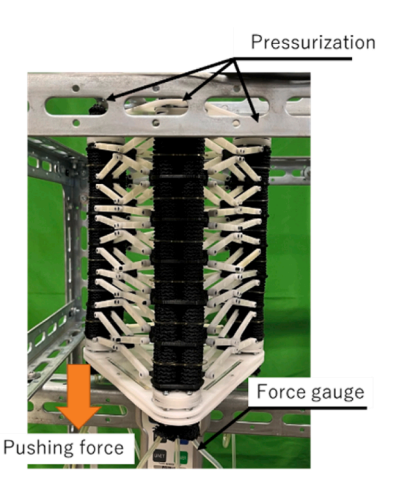


Fig. 10. Appearance of the experimental setup used to measure the generated force.

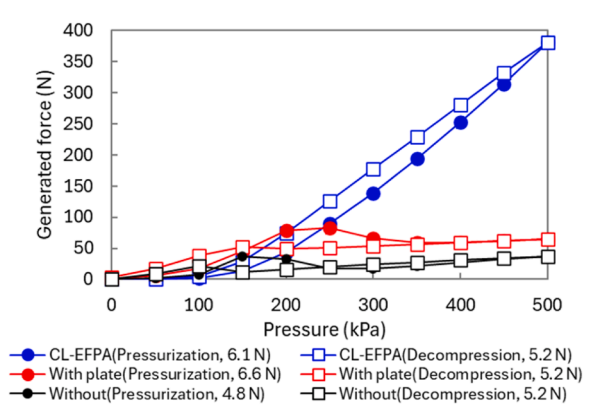


Fig. 11. Relationship between the pressure and generated force of each actuator.

generated by the CL-EFPA could be measured without buckling. The maximum generated force in the CL-EFPA was approximately 380 N (which was 10 times larger than that of the integrated EFPA without the plate). The CL-EFPA exhibited a minor hysteretic response. This is because, when the actuator was pressurized and then depressurized, the EFPA did not return to its original size but became slightly larger.

3.3. Characteristics of bending stiffness in soft actuators

The effects of plate and link mechanisms on the bending stiffness of each soft actuator were verified. Fig. 12(a) shows the experimental setup used to investigate the bending stiffness. During the experiment, a force gauge was connected to the top end of the actuator using a string, and the force gauge was pulled. The pulling force was measured using a force gauge, and the deflection displacement at the top end of the actuator was measured using a scale. These experiments were repeated five times at supply pressures ranging from 0 to 500 kPa, in increments of $100 \, \text{kPa}$.

Fig. 12 (b) to (d) show the relationship between the deflection/length ratio and generated force (pulling force). Fig. 12 (b) to (d) show the results of the integrated EFPA without a large plate, integrated EFPA with a large plate, and proposed CL-EFPA, respectively. In each figure, the symbols denote variations in the supply pressure. The values in the legend of Fig. 12 (b) to (d) represent the moment arms corresponding to the height of the actuator. The deflection/length ratio indicates the length of each actuator at the corresponding supply pressure. The following can be observed in these figures: The pulling force (generated force) is directly proportional to the deflection/length ratio. This is similar to the characteristics of the spring and material, and the slope is

(a) Experimental setup used to measure the bending stiffness.

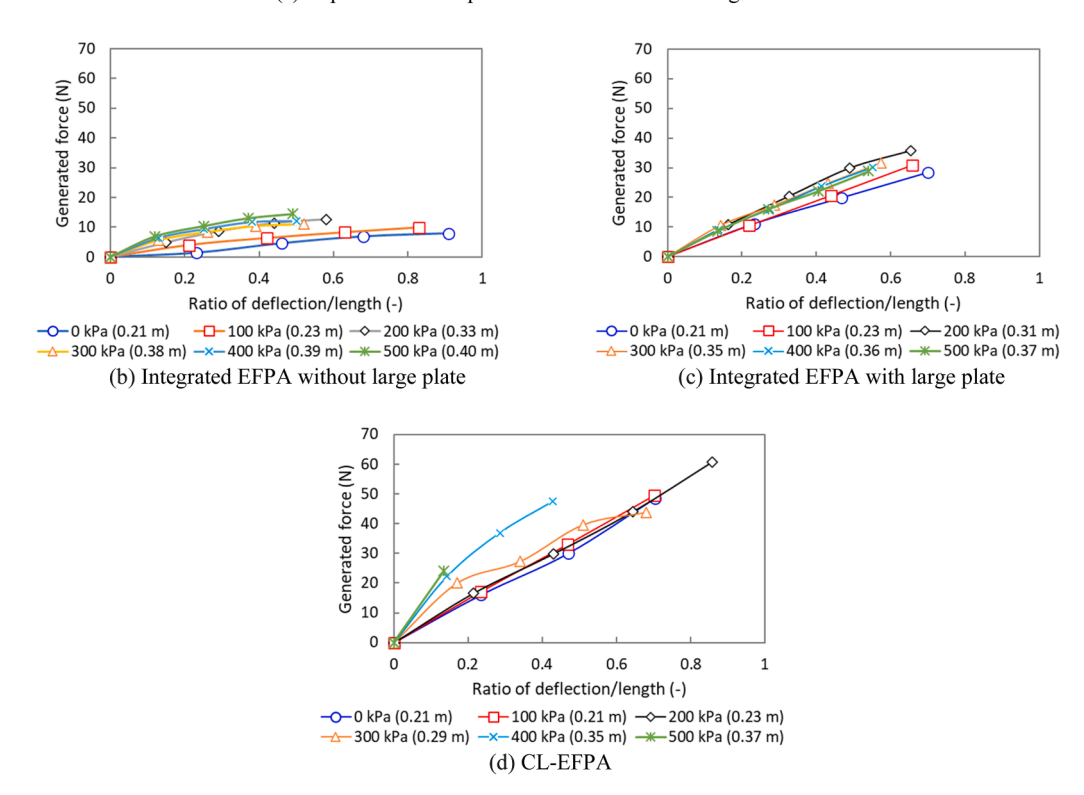


Fig. 12. Relationship between the ratio of deflection/length and bending stiffness.

the Young's modulus, which corresponds to the bending stiffness of the actuator. In addition, as the supply pressure increased, the generated force increased slightly. This implies that the Young's modulus of the entire actuator increased as the silicone rubber tube in the EFPA expanded. The bending stiffness values shown in Fig. 12 (b) to (d) were 18, 52, and 74 N/(-), respectively. Therefore, the bending stiffness of the soft actuator can be enhanced by the three-dimensional restraints rather than by plane restraints using plates (1.4 times as large as the plate-integrated EFPA). However, the mechanisms underlying the enhanced generated force and bending stiffness have not been clarified theoretically. In future studies, a theoretical model of the mechanism using three-dimensional and plane restraints must be developed.

As shown in Fig. 12 (d), the generated force could not be measured because of the damage to the actuator when supply pressures of 400 or 500 kPa were applied. This damage was caused by breakage of the link mechanism using a typical material of the poly-lactic acid (PLA). The improvement of the link mechanism will be our future work. Furthermore, the slope in Fig. 12 (d) changes considerably at a supply pressure of 400 kPa. The bending stiffness at these two pressures was approximately 70 and 123 N/(-), respectively (2.4 times as large as the previous one with the plate). It is believed that the bending stiffness of each EFPA increased when deformed by changing the angle between the link mechanisms. Therefore, it is expected that the bending stiffness of the

CL-EFPA can be enhanced by three-dimensional restraints, the structure of the link mechanism, and the number of pitches inserted.

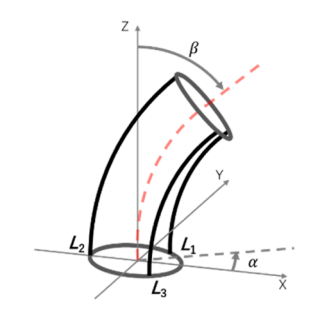
4. Analytical model of CL-EFPA for attitude control

4.1. Analytical model of CL-EFPA

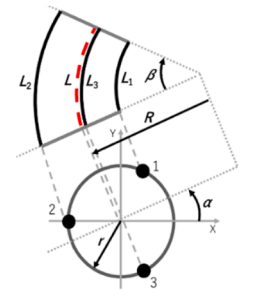
An analytical model for attitude control is required to control the extension and bending motions. Therefore, the feasibility of attitude control for the CL-EFPA using the proposed analytical model was verified [39]. Fig. 13 shows the analytical model used for the attitude control of the CL-EFPA. In the analytical model, each EFPA was assumed to have an arc shape when CL-EFPA was bent, as shown in Fig. 13. The bending direction angle α and bending angle β are defined as shown in Fig. 13 (a), respectively. We denote the three EFPAs as EFPA 1, EFPA 2, and EFPA 3 counterclockwise from the x-axis, as shown in Fig. 13 (b). Their lengths are denoted as L_1 , L_2 , and L_3 , respectively.

From these definitions, the following equations can be obtained from the geometric relationship [39]:

$$L_1 = \left\{ R - r \cos\left(\frac{\pi}{3} - \alpha\right) \right\} \beta \tag{1}$$



(a) Angles α and β for bending motion



(b) Relationship of length of EFPAs

Fig. 13. Analytical model for the attitude control of the CL-EFPA.

$$L_2 = \{R - r\cos(\pi - \alpha)\}\beta \tag{2}$$

$$L_3 = \left\{ R - r \cos \left(\frac{5\pi}{3} - \alpha \right) \right\} \beta \tag{3}$$

$$L = \frac{L_1 + L_2 + L_3}{3} \tag{4}$$

$$R = \frac{L}{\beta} \tag{5}$$

where L, r, and R are the central length of the CL-EFPA, distance (90 mm) between the origin and central EFPA, and radius of curvature, respectively.

The attitude of the actuator is determined by the bending direction angle α , bending angle β , and center line length L. Therefore, in the attitude control, after these target values are given, and the lengths L_1 , L_2 , and L_3 of EFPA are calculated using Eqs. (1), (2), (3), and (5). The desired attitude can then be obtained by varying the pressure of each EFPA and controlling its length. Using Eqs. (1), (2), (3), and (5), the bending direction angle α and the bending angle β can be obtained as follows:

$$\alpha = \tan^{-1} \frac{\sqrt{3}(L_3 - L_1)}{2L_2 - L_1 - L_3} \tag{6}$$

In the calculation, when the numerator is negative, 2π is added to the value calculated by Eq. (6), so that the value of α will be in the range of $0-2\pi$.

$$\beta = \frac{L_2 - L}{r \bullet \cos \alpha} \tag{7}$$

When $\cos \alpha = 0$ in Eq. (7), from Eqs. (1) and (3), it can be observed that β can be calculated by the following equation.

$$\beta = \frac{|L_3 - L_1|}{\sqrt{3} \bullet r} \tag{8}$$

Using these equations and Eq. (4), angles α and β , and length L (which determines the posture of the actuator), the lengths L_1 , L_2 , and L_3 can be obtained while controlling.

For attitude control, the proposed analytical model can be expressed as follows: First, the desired attitude is given by three parameters: the bending direction angle α , bending angle β , and center line length L. Second, using Eqs. (1), (2), (3), and (5), the three desired lengths, L_1 , L_2 , and L_3 , and feedback control can be performed using these values and the measured EFPA lengths. Using Eqs. (4), (6), (7), (8) and measured lengths L_1 , L_2 , and L_3 , the controlled angles α , β , and length L are calculated and compared with their desired values.

Finally, to verify the validity of the proposed analytical model, a comparison of the calculated and experimental results for the bending angle is shown in Fig. 14. In the figure, the measured values shown by red squares were obtained from a photograph of the actuator posture, and the values were calculated using the measured lengths of the three

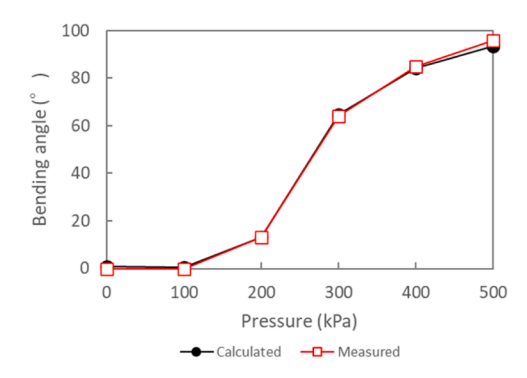


Fig. 14. Comparison of measured and calculated bending angles.

EFPAs and an analytical model. As shown in the figure, the calculated results for the bending angle agree well with the experimental results, indicating that the analytical model is valid.

4.2. Attitude control system of CL-EFPA

Fig. 15 shows a schematic of the attitude control system of the proposed soft actuator. The system consisted of a CL-EFPA with ten pitches, an embedded controller using a microcomputer (Espressif Systems Co. Ltd., ESP32), three quasi-servo valves to control the internal pressures of the EFPAs, and three wire-type potentiometers to measure the displacement of the EFPAs. The quasi-servo valve consisted of two on/off control valves (KOGANEI Co. Ltd., G010E1) and had a switching function to supply or exhaust as well as a variable fluid function that could adjust the output flow rate [40]. A wire-type potentiometer was placed on top of the CL-EFPA, and the wire was connected to the bottom through a small hole in each constraint plate at the center of the integrated EFPA actuator, as shown in the right side of Fig. 15. Therefore, the center displacement of each integrated EFPA could be measured even if the actuator deformed into a bent shape [35].

Attitude control of the system was performed as follows: The embedded controller calculated the displacement of the centerline of each EFPA using wire-type linear potentiometers and an analog-to-digital (A/D) converter. The deviation from the reference displacement was calculated using a controller. As mentioned in Section 4.1, the reference displacements were obtained using the bending direction angle α , bending angle β , and centerline length L of the desired posture, and by calculating the lengths of each EFPA using Eqs. (1), (2), (3), and (5). The control input for each quasi-servo valve was calculated based on the following PID control scheme:

$$u_{i(j)} = k_P \bullet e_{i(j)} + k_I \sum_{i(j)} e_{i(j)} + k_D (e_{i(j)} - e_{i(j-1)})$$
(9)

 $u_{i(j)} > 0$ Switching valve : Supply $u_{i(j)} \leq 0$ Switching valve : Exhaust

(10)

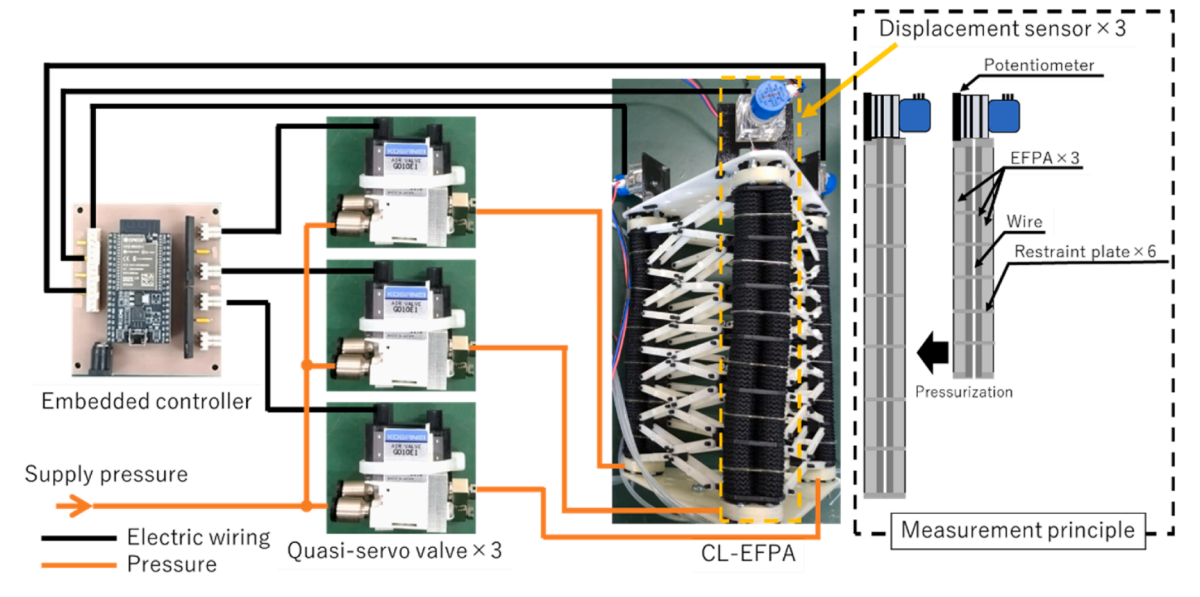


Fig. 15. Schematic of the attitude control system.

$$u_{i(j)d} = |u_{i(j)}| + 22.5. (11)$$

where $u_{i(j)}$, $e_{i(j)}$, k_P , k_I , and k_D denote the incremental changes in the duty ratio of each valve, error between the desired displacement of each EFPA and the controlled displacement, proportional gain, integral gain, and differential gain, respectively. The control gain was determined using the transient response method. Consequently, gains k_P of 21.2, k_I of 19.6, and k_D of 7.18 [%/mm] were obtained. In this case, i is an index referring to EFPAs, and $u_{i(j)d}$ denotes the input duty ratio, which is increased by 22.5 % to compensate for the dead zone.

Fig. 16 shows the transient response of the displacement for each

EFPA. Fig. 17 shows a transient view of the attitude control of the CL-EFPA. As shown in Fig. 16, each color represents the controlled displacement of each EFPA when loads are applied to the top end of the CL-EFPA. The reference of the bending direction angle α , bending angle β , and centerline length L were set as 14.4 °/s, 60°, and 330 mm, respectively. A supply pressure of 500 kPa was applied to the quasi-servo valves. This target motion, in which the top end of the CL-EFPA followed a circular trajectory, was chosen considering wrist and shoulder rehabilitation exercises. The results indicated that the controlled displacement of each EFPA without a load could accurately trace each reference. It was also discovered that each error increased when the EFPA

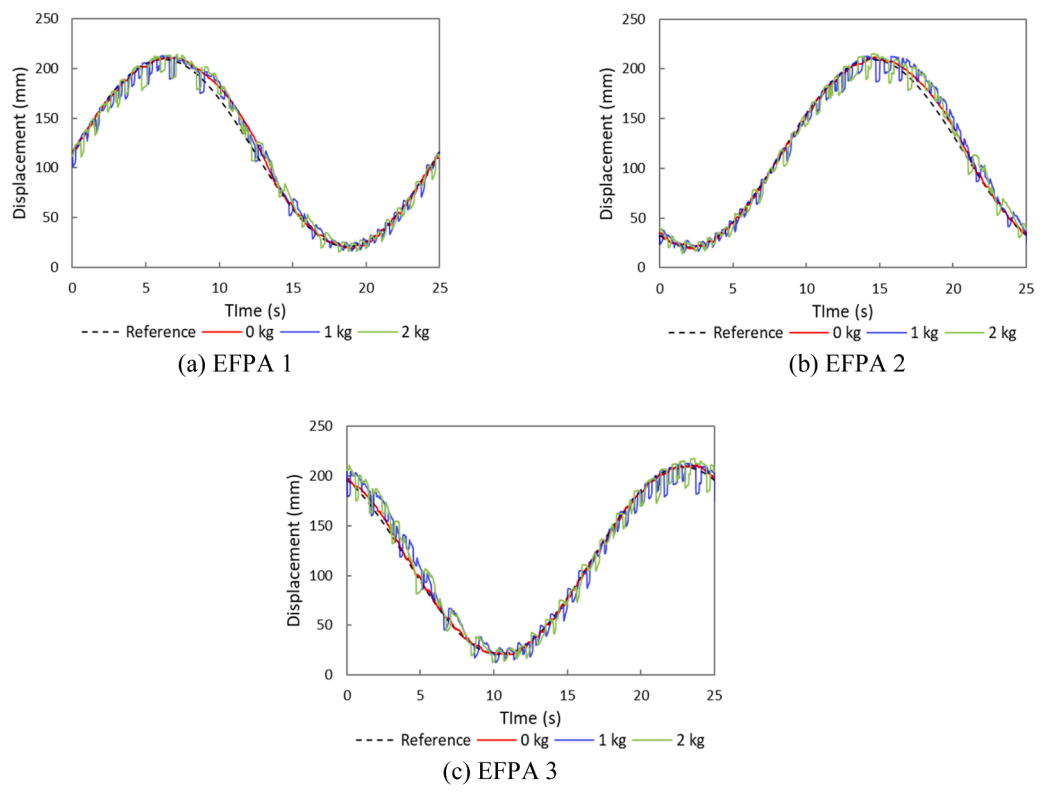


Fig. 16. Transient response of displacement of each EFPA.



Fig. 17. Transient view of the attitude control of the CL-EFPA.

decompressed. This is because the exhaust speed of the quasi-servo valve was lower than the supply speed. The maximum displacement error during the decompression was approximately $19.7~\mathrm{mm}$ (9.3~% of the maximum displacement).

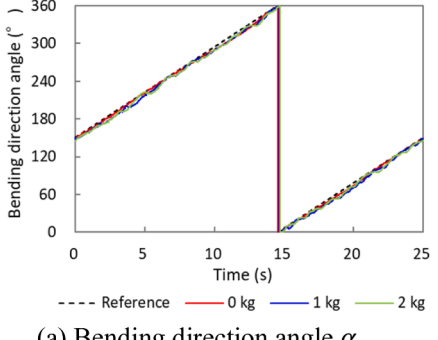
In the attitude control experiment with loads, it was demonstrated that the controlled displacement of the actuator exhibited oscillatory behavior with increasing loads. This oscillatory behavior became more pronounced under pressurization (the maximum displacement was approximately 25.3 mm). However, it can be observed that the controlled displacement of each EFPA could generally trace each reference without a phase delay.

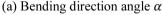
Fig. 18 (a), (b), and (c) show the transient responses of the desired attitude, which are the desired bending direction angles α and β , and desired centerline length L, respectively. These values were calculated using the measured EFPA lengths and Eqs. (4) and (6)–(8). Fig. 18 (a) shows that the controlled bending direction angles are in good agreement with the desired angles. Fig. 18 (b) and (c) show that the maximum error between the desired and controlled bending angles without loads was 7.0 % and that of the centerline length was 2.1 %.

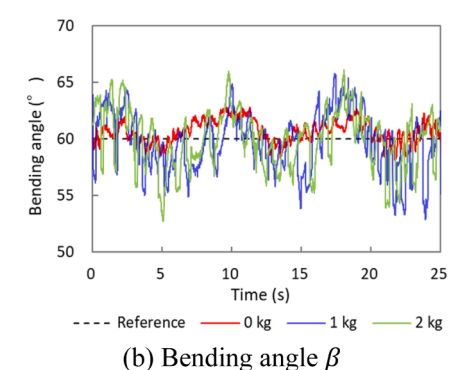
To investigate the dynamics of the attitude control system, including the CL-EFPA, a frequency response experiment was performed in the range 0.025–0.2 Hz. Fig. 19 shows a Bode diagram of the CL-EFPA when attitude control was performed at several frequencies. The upper and lower part of Fig. 19 show the gain and phase plots, respectively. The upper part of Fig. 19 shows that the bandwidth frequency of the attitude control system was approximately 0.086 Hz. From the lower part of Fig. 19, it can be observed that the 90° phase difference frequency was 0.17 Hz. However, it is difficult to apply this system to robot arms in the industry. Conversely, the application of the proposed system as an assistive exercise or rehabilitation device can be considered as follows: This system can be applied to devices that require a larger generated force and do not require high-frequency operations. One method for improving the dynamics of the proposed system is to use a servo valve with a higher flow rate and response.

5. Conclusions

In this study, we proposed and tested a CL-EFPA with a larger







350 340 330 320 310 0 5 10 15 20 25 Time (s) ---- Reference 0 kg 1 kg 2 kg

(c) Centerline length L

Fig. 18. Transient responses of angles α , β , and length L of the CL-EFPA.

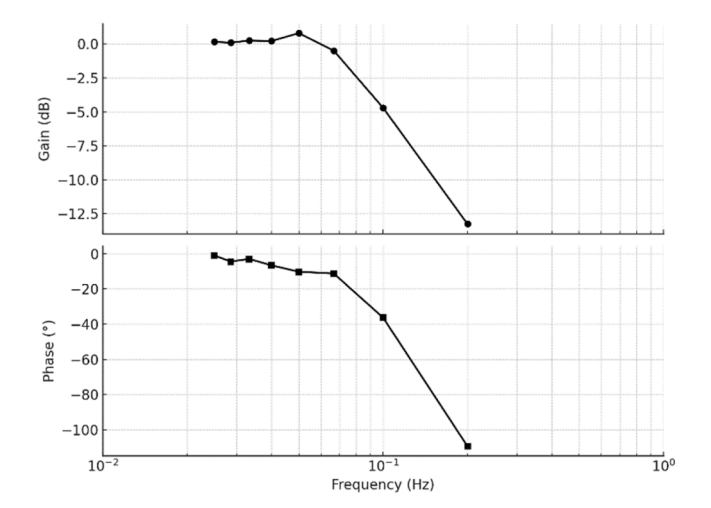


Fig. 19. Bode diagram of the attitude control system.

generated force and backdrivability using a cross-link mechanism that can be restrained in 3D. The CL-EFPA is less likely to buckle because the surrounding EFPAs are pulled by the link mechanism. Consequently, the actuator achieved a generated force of 380 N, despite each EFPA having high flexibility. In addition, it was confirmed that the proposed CL-EFPA could perform bending motions as well as extensions.

The generated force and bending stiffness of the CL-EFPA were compared with those of previous EFPAs. The generated force of the CL-EFPA was enhanced by 3.8 times without buckling compared to that of the previous EFPA with plates. The bending stiffness of the proposed actuator increased considerably when the supply pressure exceeded 400 kPa. Therefore, the stiffness of the actuator was enhanced by approximately 2.4 times compared with the previous one.

To perform any bending motion, the attitude control of the CL-EFPA using an analytical model and an embedded controller was proposed and tested. The results confirmed that the controlled attitudes agreed well with the desired attitudes. The frequency response of the proposed control system was also investigated. Consequently, the bandwidth frequency of the attitude control system was approximately 0.086 Hz. In addition, it was discovered that the 90° phase difference frequency was 0.17 Hz. It is expected that this system can be applied to assistive and rehabilitation devices with high force generation.

In future studies, a theoretical study of the mechanism to increase the generated force in the CL-EFPA with three-dimensional restraints will be thoroughly investigated. Robotic arms and rehabilitation devices can also be developed based on the theoretical studies of enhancement mechanisms.

Declaration of Competing Interest

We declare that We have no conflicts of interest to disclose regarding this manuscript. This research was conducted without any commercial or financial relationships that could be construed as a potential conflict of interest. We have no financial interests in any products, services, or organizations mentioned in this paper. This research was conducted without any biases or influences that may have affected the results or interpretation of the findings.

Acknowledgements

This work was supported by Science and Technology Research Grants from the Suzuki Foundation and the Wesco Foundation. We would like to thank Editage (www.editage.jp) for the English language editing.

References

- P.H. Guyen, W. Zhang, Design and computational modeling of fabric soft pneumatic actuators for wearable assistive devices, Sci. Rep. 10 (2020) 9638, https://doi.org/10.1038/s41598-020-65003-2.
- [2] M. Pan, C. Yuan, X. Liang, et al., Soft actuators and robotic devices for rehabilitation and assistance, Adv. Intell. Syst. 4 (2022) 2100140, https://doi.org/ 10.1002/aisv.202100140.
- [3] M. Xavier, C. Tawk, A. Zolfagharian, et al., Soft pneumatic actuators: a review of design, fabrication, modeling, sensing, control and applications, IEEE Access 10 (2022) 59442–59485, https://doi.org/10.1109/ACCESS.2022.3179589.
- [4] M. Li, A. Pal, A. Aghakhani, et al., Soft actuators for real-world applications, Nat. Rev. Mater. 7 (2022) 235–249, https://doi.org/10.1038/s41578-021-00389-7.
- [5] R. Kobayashi, H. Nabae, G. Endo, et al., Soft tensegrity robot driven by thin artificial muscles for the exploration of unknown spatial configurations, IEEE Robot. Autom. Lett. 7 (2022) 5349–5356, https://doi.org/10.1109/ LRA_2022_3153700.
- [6] D.R. Yao, I. Kim, S. Yin, et al., Multimodal soft robotic actuation and locomotion, Adv. Mater. 36 (2024) 2308829, https://doi.org/10.1002/adma.202308829.
- [7] T. Nakamura, Fluid-driven soft actuators for soft robots, J. Robot. Mechatron. 36 (2024) 251–259, https://doi.org/10.20965/jrm.2024.p0251.
- [8] D. Bruder, X. Fu, R.B. Gillespie, et al., Koopman-based control of a soft continuum manipulator under variable loading conditions, IEEE Robot. Autom. Lett. 6 (2022) 6852–6859. https://doi.org/10.1109/LRA.2021.3095268.
- [9] H. Tomori, T. Nakamura, Theoretical comparison of McKibben-type artificial muscle and novel straight-fiber-type artificial muscle, Int. J. Autom. Technol. 5 (2011) 544–550. https://doi.org/10.20965/jiat.2011.p0544.
- [10] Y. Feng, T. Ide, H. Nabae, et al., Safety-enhanced control strategy of a power soft robot driven by hydraulic artificial muscles, Robomech J. 8 (2021) 10, https://doi. org/10.1186/s40648-021-00194-5.
- [11] T. Noritsugu, M. Takaiwa, D. Sasaki, Development of power assist wear using pneumatic rubber artificial muscles, J. Robot. Mechatron. 21 (2009) 607–613, https://doi.org/10.20965/jrm.2009.p0607.
- [12] E.W. Hawkes, D.L. Christensen, A.M. Okamura, Design and implementation of a 300% strain soft artificial muscle, 2016 IEEE Int. Conf. on Robot. Automation (2016) 4022–4029. https://doi.org/10.1109/ICRA.2016.7487592.
- [13] W. Wang, Y. Zhu, S. Cai1, G. Bao, Ultralong stretchable soft actuator (US²A): design, modeling and application, Chn. J. Mechan. Eng. 36 (2023) 13, https://doi. org/10.1186/s10033-023-00835-3
- [14] K. Han, N.H. Kim, D. Shin, A novel soft pneumatic artificial muscle with highcontraction ratio, Soft Robot. 5 (2018) 554–556, https://doi.org/10.1089/ soro.2017.0114.
- [15] E.W. Hawkes, L.H. Blumenschein, J.D. Greer, A.M. Okamura, A soft robot that navigates its environment through growth, Sci. Robot. 2 (2017) 3028, https://doi. org/10.1126/scirobotics.aan3028.
- [16] H.D. Yang, B.T. Greczek, A.T. Asbeck, Modeling and analysis of a High-Displacement pneumatic artificial muscle with integrated sensing, Front. Robot. AI 5 (2019) 136, https://doi.org/10.3389/frobt.2018.00136.
- [17] R.V. Martinez, C.R. Fish, X. Chen, et al., Elastomeric origami: programmable paperelastomer composites as pneumatic actuators, Adv. Funct. Mater. 22 (2012) 1376–1384, https://doi.org/10.1002/adfm.201102978.
- [18] G. Agarwal, N. Besuchet, B. Audergon, et al., Stretchable materials for robust soft actuators towards assistive wearable devices, Sci. Rep. 6 (2016) 34224, https:// doi.org/10.1038/srep34224.
- [19] E.H. Skorina, M. Luo, W.Y. Oo, et al., Reverse pneumatic artificial muscles (rPAMs): modeling, integration, and control, Plos One 13 (2018) e0204637, https://doi.org/10.1371/journal.pone.0204637.
- [20] O. Azami, D. Morisaki, T. Miyazaki, et al., Development of the extension type pneumatic soft actuator with built-in displacement sensor, Sens. Actuators A Phys. 300 (2019) 111623, https://doi.org/10.1016/j.sna.2019.111623.
- [21] W. Chen, C. Xiong, C. Liu, et al., Fabrication and dynamic modeling of bidirectional bending soft actuator integrated with optical waveguide curvature sensor, Soft Robot. 6 (2019) 495–506, https://doi.org/10.1089/soro.2018.0061.
- [22] J. Zhang, J. Zhou, Z.K. Cheng, S. Yuan, Fabrication, mechanical modeling, and experiments of a 3D-Motion soft actuator for flexible sensing, IEEE Access 8 (2020) 159100–159109, https://doi.org/10.1109/ACCESS.2020.3017447.
- [23] P. Cheng, Y. Lu, C. Wu, et al., Reconfigurable bionic soft pneumatic gripper for fruit handling based on shape and size adaptation, J. Phys. D: Appl. Phys. 56 (2023) 044003, https://doi.org/10.1088/1361-6463/aca811.
- [24] C. Alessi, E. Falotico, A. Lucantonio, Ablation study of a dynamic model for a 3D-printed pneumatic soft robotic arm, IEEE Access 11 (2023) 37840–37853, https://doi.org/10.1109/ACCESS.2023.3266282.
- [25] K.H. Heung, T. Lei, K. Liang, et al., Quasi-static modeling framework for soft bellow-based biomimetic actuators, Biomimetics 9 (2024) 160, https://doi.org/ 10.3390/biomimetics9030160
- [26] L. Fracczak, M. Nowak, K. Koter, Flexible push pneumatic actuator with high elongation, Sens. Actuators A Phys. 321 (2021) 112578, https://doi.org/10.1016/ i.sna.2021.112578.
- [27] Z. Qiu, S. Zhang, Y. Xue, et al., An empirical model of soft bellows actuator, Sci. Rep. 14 (2024) 28681, https://doi.org/10.1038/s41598-024-79084-w.
- [28] D. Malas, G. Zhang, S. Wang, et al., Fluidic multichambered actuator and multiaxis intrinsic force sensing, Soft Robot. 12 (2025) 81–93, https://doi.org/10.1089/ soro.2023.0242.
- [29] M. Keyvanara, A. Goshtasbi, I.A. Kuling, A geometric approach towards inverse kinematics of soft extensible pneumatic actuators intended for trajectory tracking, sensors 23 (2023) 6882, https://doi.org/10.3390/s23156882.

- [30] Y. Yu, T. Fu, Design and experimental study of cavity structure of pneumatic soft actuator, actuators 12 (2023) 314, https://doi.org/10.3390/act12080314.
- [31] T. Kanno, S. Ohkura, O. Azami, et al., Model of a Coil-Reinforced cylindrical soft actuator, Appl. Sci. 9 (2019) 2109, https://doi.org/10.3390/app9102109.
- [32] H. Lia, J. Yao, P. Zhou, et al., High-force soft pneumatic actuators based on novel casting method for robotic applications, Sens. Actuators A Phys. 306 (2020) 111957, https://doi.org/10.1016/j.sna.2020.111957.
- [33] Kazuki Higashi, Keisuke Koyama, Ryuta Ozawa, et al., Torque-Sensing soft bellows actuator for Multi-Fingered hands taking Bellow's buckling into consideration, IEEE Access 11 (2023) 129258–129268, https://doi.org/10.1109/ ACCESS.2023.3333385.
- [34] M. Abboodi, M. Doumit, Development and testing of novel soft sleeve actuators, IEEE Access 12 (2024) 39995–40010, https://doi.org/10.1109/ ACCESS.2024.3376407.
- [35] S. Shimooka, T. Akagi, S. Dohta, et al., Development of reinforced extension type flexible pneumatic actuator with circumferential restraints and its application for rehabilitation device, Int. J. Automot. Mech. Eng. 17 (2020) 8116–8127, https:// doi.org/10.15282/ijame.17.3.2020.05.0609.
- [36] B. Yu, J. Yang, R. Du, Design and Implementation of a Scissor-mechanism-based Vacuum Powered Actuator, Prof. The 2020 IEEE Int. conf. Real-time Computing and Robo. (2020), 177–182, https://doi.org/10.1109/RCAR49640.2020.9303323
- [37] J. Lee, A. Coutinho, N. Oh, et al., Vacuum-Driven Class-2 Tensegrity-Based mechanism for quadrupedal robot motion, IEEE Robot. Autom. Lett. 9 (2024) 6520–6527, https://doi.org/10.1109/LRA.2024.3407410.
- [38] Y. Yoshimitsu, S. Ikemoto, Development of tensegrity manipulator driven by 40 pneumatic cylinders for investigating functionality in Hyper-Redundant musculoskeletal systems, J. Robot. Mechatron. 35 (2023) 1366–1373, https://doi.org/10.20965/jrm.2023.p1366.

- [39] M. Aliff, S. Dohta, T. Akagi, Control and analysis of robot arm using flexible pneumatic cylinder, Mech. Eng. J. 1 (2014) DR0051, https://doi.org/10.1299/ mei.2014dr0051.
- [40] Y. Moriwake, T. Akagi, S. Dohta, et al., Development of low-cost pressure control type quasi-servo valve using embedded controller, J. Proc. Eng. 41 (2012) 493–500, https://doi.org/10.1016/j.proeng.2012.07.203.

So Shimooka received the B.S and M.S and Dr. Eng. degrees in intelligent mechanical engineering from Okayama University of Science in 2014, 2016, and 2020, respectively. Then he worked as an assistant professor in National Institute of Technology, Matsue College. He is currently an assistant professor in Faculty of Environmental, Life, Natural Science and Technology at Okayama University. His research interests are mechatronics and welfare and mechanical engineering.

Kazuma Tadachi is with Mechanical and Systems Engineering Program, Okayama University.

Tetsushi Kamegawa received his B.S., M.S., and Ph.D. degrees in engineering from the Tokyo Institute of Technology, Japan, in 1999, 2001, and 2004, respectively. In 2004, he was a visiting scholar at Roma University, Italy. From 2004–2006, he was a researcher at the International Rescue System Institute, Japan. From 2006–2024, he worked as a research associate, assistant professor, senior assistant professor and associate professor at Okayama University, Japan. He was also a visiting researcher at Carnegie Mellon University in 2012. He became a professor in the Faculty of Environmental, Life, Natural Science and Technology at Okayama University in 2024. His research interests include snake robots, rescue robots, and medical robots.